

Contents lists available at ScienceDirect

Petroleum Science

journal homepage: www.keaipublishing.com/en/journals/petroleum-science



Original Paper

Changes in shale microstructure and fluid flow under high temperature: Experimental analysis and fluid—structure interaction simulation



Xiang-Ru Chen $^{a, \, b}$, Xin Tang $^{a, \, *}$, Rui-Gang Zhang c , Heng Yang d , Qiu-Qi Chen a , Zhang-Ping Yan a , Lei Zhang a

- ^a School of Civil Engineering, Chongqing Three Gorges University, Chongqing, 404199, PR China
- ^b China University of Geosciences, Beijing, 100083, PR China
- ^c China University of Mining & Technology, Xuzhou, 221006, Jiangsu, PR China
- ^d Daqing Oilfield Exploration and Development Institute, Daqing, 163100, Heilongjiang, PR China

ARTICLE INFO

Article history: Received 1 October 2024 Received in revised form 27 February 2025 Accepted 28 February 2025 Available online 1 March 2025

Edited by Yan-Hua Sun

Keywords:
High temperature treatment
Oil shale
Longmaxi Formation
Fluid—structure interaction
Fluid simulation

ABSTRACT

Oil shale is characterized by a dense structure, low proportion of pores and fissures, and low permeability. Pore-fracture systems serve as crucial channels for shale oil migration, directly influencing the production efficiency of shale oil resources. Effectively stimulating oil shale reservoirs remains a challenging and active research topic. This investigation employed shale specimens obtained from the Longmaxi Formation. Scanning electron microscopy, fluid injection experiments, and fluid-structure interaction simulations were used to comprehensively analyze structural changes and fluid flow behavior under high temperatures from microscopic to macroscopic scales. Experimental results indicate that the temperature has little effect on the structure and permeability of shale before 300 °C. However, there are two threshold temperatures within the range of 300 to 600 °C that have significant effects on the structure and permeability of oil shale. The first threshold temperature is between 300 and 400 °C, which causes the oil shale porosity, pore-fracture ratio, and permeability begin to increase. This is manifested by the decrease in micropores and mesopores, the increase in macropores, and the formation of a large number of isolated pores and fissures within the shale. The permeability increases but not significantly. The second threshold temperature is between 500 and 600 °C, which increases the permeability of oil shale significantly. During this stage, micropores and mesopores are further reduced, and macropores are significantly enlarged. A large number of connected and penetrated pores and fissures are formed. More numerous and thicker streamlines appear inside the oil shale. The experimental results demonstrate that high temperatures significantly alter the microstructure and permeability of oil shale. At the same time, the experimental results can provide a reference for the research of in-situ heating techniques in oil shale reservoir transformation.

© 2025 The Authors. Publishing services by Elsevier B.V. on behalf of KeAi Communications Co. Ltd. This is an open access article under the CC BY-NC-ND license (http://creativecommons.org/licenses/by-nc-nd/4.0/).

1. Introduction

Shale oil, as an important unconventional energy source, is playing an increasingly significant role in the global energy mix. With the gradual depletion of conventional oil and gas resources, shale oil has become an important part of countries' energy strategies. Shale oil is abundant and widely distributed, especially in

regions such as North America, Europe, and China (Bera and Babadagli, 2015; Kang et al., 2020, 2023; Pan et al., 2024; Wang et al., 2024). However, the extraction process faces enormous technical challenges due to the dense and complex structure, high heterogeneity, low porosity, and low permeability of shale. The mining process presents enormous technical challenges. At the same time, these factors have led to the high cost and relatively low efficiency of shale oil extraction. There is an urgent need to improve its economics and sustainability through technological innovation (Lei et al., 2021; Li et al., 2009; Spigolon et al., 2015; Zhou et al.,

E-mail address: tangxin@cumt.edu.cn (X. Tang).

^{*} Corresponding author.

2019; Zou et al., 2022).

Currently, there are two main methods of extracting shale oil: surface extraction and underground in-situ extraction (Altun et al., 2006; Han et al., 2014; Jiang et al., 2007; Wang et al., 2012). Surface mining is dominated by oil shale retorting technology. For example, the Fushun retorting process in China, the Petrosix technology in Brazil and the Kixiter technology in Estonia have all been widely used in industrial production. However, oil shale retorting technology causes severe environmental pollution. Studies indicate that producing 1 tonne of shale oil generates approximately 25 tonnes of solid waste residues and 4 tonnes of wastewater, accompanied by toxic gas emissions. These pollutants critically damage vegetation ecosystems, contaminate groundwater systems, deteriorate air quality, and pose significant health risks to humans in mining regions (Gavrilova et al., 2010; Pan et al., 2012; Trikkel et al., 2008; Velts et al., 2008). The underground insitu heating technology has emerged accordingly (Fig. 1). In-situ extraction technique refers to the direct pyrolysis of oil shale within the target reservoir. High-temperature treatment induces extensive pore-fracture in the oil shale, which significantly accelerates heat transfer processes. The kerogen inside the oil shale is pyrolysed at high temperatures to produce oil and gas (Han et al., 2019; Lin et al., 2016; Saif et al., 2017; Wang et al., 2020, 2021; Yang et al., 2016). In-situ extraction technology has emerged as the dominant approach for contemporary shale oil exploitation, owing to its integrated advantages including streamlined operational workflows, environmentally sustainable characteristics, and compatibility with deep reservoirs. These technical merits position it as the strategic pathway for future oil shale development (Burnham, 2018; Kang et al., 2018; Kim et al., 2020; Lee et al., 2017; Liu et al., 2018). However, the extreme heterogeneity of oil shale complicates the understanding of structural changes and fluid flow patterns under high temperatures, necessitating further research.

There has been a certain research base on the study of the effect of temperature on oil shale. Among them, there are more studies about the effect of temperature on shale mechanics properties. Several scholars have carried out uniaxial compression experiments, triaxial compression experiments and numerical simulations on rocks with different lithologies or shales with different laminar angles to investigate the changes of mechanical properties of rocks under the effect of temperature. In addition, different

heating methods have different effects on the structure of shale. Wang et al. (2021) investigated the permeability of oil shale by means of permeability test and flow field simulation experiment, which revealed the permeability changes and pyrolysis characteristics of oil shale under high temperature water vapor heating. Chang et al. (2024) analysed the surface morphology and microstructure of type I fracture in Longmaxi Formation shale using scanning electron microscopy and white light interferometry based on cyclic thermal shock and high-temperature acid-etching experiments, which provides a new research method for reducing the cracking pressure in deep shale formations. Zhu et al. (2022) analysed the effect of inlet temperature, total organic carbon (TOC) and confined area on the recovery using a high temperature nitrogen injection in-situ conversion process (HNICP) in the Songliao Basin, China. The above studies show that previous work has laid a solid foundation for in-situ extraction technology. However, few studies have comprehensively characterised the structural changes and fluid flow of shale under high temperature based on pore morphology changes, pore size distribution, and coupled flow-structure simulations.

This paper is based on previous research results (Chen et al., 2024). The organic-rich shale from the Longmaxi Formation is studied in this paper. Scanning electron microscopy and fluid injection experiments were used to characterise the changes in the pore structure of shale. Additionally, the microstructural changes of shale under high temperature were clarified. A three-dimensional rock model was reconstructed using CT data and digital core technology, and fluid—structure interaction simulations were carried out. The changes in fluid flow behavior in shale under high temperature were revealed, providing a new perspective for the insitu heating technology of oil shale.

2. Shale samples and experimental methods

2.1. Shale sample preparation

Samples were collected from the outcrop of Longmaxi Formation, Longtan Town, Youyang Tujia and Miao Autonomous County, Chongqing, China. The specific latitude and longitude are $108^{\circ}52'48.482''$ east longitude and $28^{\circ}38'51.727''$ north latitude. The shale of this formation belongs to the high maturity shale, and the vitrinite reflectance (R_0) is 2.56%. The total organic content

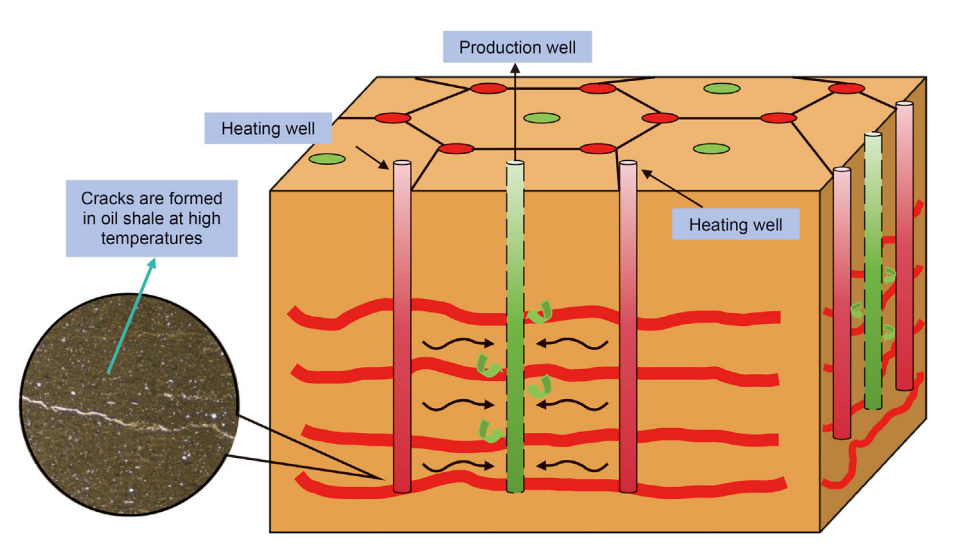


Fig. 1. In-situ conversion process (ICP) technology proposed by Shell (USA).

(TOC) is 3.18%. Quartz, calcite, clay minerals, plagioclase and other minerals account for 29.8%, 30.3%, 32.3%, 5.8% and 1.8%, respectively (Fig. 2). Fresh outcrops with intact rock structure and no obvious fractures and impurities were selected to prepare the samples required for the experiment. The shale samples were crushed by artificial physical crushing. Seven massive shale samples with length, width and height less than 1 cm were prepared, which were named LMX-KS, LMX-K1, LMX-K2, LMX-K3, LMX-K4, LMX-K5, and LMX-K6, respectively. Powdered shale samples with particle sizes between 150 and 200 µm were screened out by standard inspection sieves, and the samples were divided into 7 groups of about 2 g each. The powder shale samples were named LMX-FS, LMX-F1, LMX-F2, LMX-F3, LMX-F4, LMX-F5, and LMX-F6, respectively. The plunger sample size is 5 cm in length and 2.5 cm in diameter (Liu et al., 2024; Sun et al., 2024, 2025; Wan et al., 2024b). Due to the complex development of shale structure and minerals, and strong heterogeneity, powder shale, massive shale, and plunger shale were all taken from the same rock.

2.2. Experimental methods

According to the results of the previous stage, temperatures above 600 °C have a negative impact on shale pore structure (Chen et al., 2024). Therefore, the heating gradient is set to normal temperature, 100, 200, 300, 400, 500, and 600 °C (Chen et al., 2024; Wan et al., 2024a; Yu et al., 2024). The experimental flow chart is shown in Fig. 3. The prepared powder shale, massive shale, and plunger shale were heated to a preset temperature in a muffle furnace at a heating rate of 30 °C/min for 6 h and then cooled naturally to room temperature (Burnham, 2016; Xu et al., 2022; Zhao et al., 2024). A JW-BK 132F specific surface instrument and an AutoPore IV high-pressure mercury instrument provided by Chongqing Three Gorges College, Chongqing, China, were used to complete fluid injection experiments, which were able to comprehensively analyse the changes in the pore structure of the shale. An Ultima IV X-ray diffractometer provided by Toppan Analytical Centre, Beijing, China, was used to conduct XRD experiments on the powdered shale, which was able to analyse the variations of the shale's mineral compositions. The argon polishing, SEM, CT, and FIB-SEM experiments were carried out at Chongqing Research Institute of Jilin University, China. A Gantan 697 argon polisher was used for argon polishing of the bulk shale samples. A ZEISS GeminiSEM 360 scanning electron microscope (SEM) and a ZEISS Xradia Context microCT were used to observe the argonpolished shale samples. A Context microCT was used to perform CT and FIB-SEM experiments on the plunger shale.

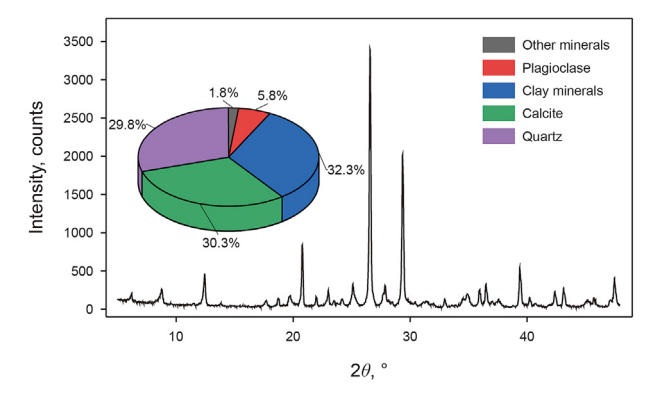


Fig. 2. Mineral composition of original sample obtained from the Longmaxi Formation shale.

3. Experimental results

3.1. Changes in the physico-chemical properties of shale

The color change of the shale after high temperature treatment is shown in Fig. 4, and the difference of shale surface change is small when the temperature is lower. Along with the temperature rise, the color of the shale surface turns from deep black to pale yellow, which is probably related to the mineral composition of the shale. The main reason for this change is the high organic matter content of shale, which is subject to pyrolysis under the high temperature treatment. At the same time, the rate of mass loss of shale under high temperatures is also changing. The mass loss rate is defined as the ratio of the reduction of shale mass to the original mass after heat treatment. As shown in Fig. 5, there are phased variations in the rate of mass loss in both plunger and powder shale. The mass loss rate of plunger shale and powder shale increases slightly before 400 °C, and increases faster after 500 °C. After the temperature reaches 400 °C, there is almost no water in the core, so the effect of water vapor on the quality of shale is negligible. The main influencing factors for the change of shale quality at this stage are a series of chemical reactions of different minerals of the core itself at high temperatures. Organic matter is constantly pyrolysed as the temperature increases (Wei and Sheng, 2022; Xiong et al., 2023). The results of XRD experiments prove that the minerals do not change much under the high temperature treatment. The proportion of calcite decreases more after 500 °C, which is caused by the high temperature induced chemical reaction of carbonatecontaining minerals to produce carbon dioxide. Therefore, the mass loss rate of shale is higher after 500 °C (Fig. 6).

3.2. Fluid injection experiments

Low-temperature carbon dioxide experiments are often used to characterise the porosity of micropores. The experiment was used to measure the amount of carbon dioxide adsorbed by shale at low temperatures. The development state of micropores can be finely characterized by comparing the differences in adsorption capacity of different samples. Fig. 7 shows that there is a large difference in the adsorption capacity of carbon dioxide for the samples after high temperature treatment. Among them, the adsorption curves of LMX-FS, LMX-F1, LMX-F2, and LMX-F3 samples are all upwardly convex, and the adsorption rate decreases with the increase of relative pressure. With the increase of temperature, the adsorption curves of LMX-F4, LMX-F5, and LMX-F6 samples were almost linearly distributed, and the adsorption rate no longer changed with the change of relative pressure. The trend of the adsorption capacity showed a wave-like change of first decreasing, then rising, and then decreasing.

The results of the low-temperature liquid nitrogen experiments showed that the type of adsorption isotherm, the type of hysteresis loop, and the amount of liquid nitrogen adsorbed by the mesopores changed significantly with increasing temperature (Fig. 8). The adsorption isothermal of samples LMX-FS, LMX-F1, LMX-F2, and LMX-F3 are all of type IV(a). The adsorption isothermal of LMX-F4, LMX-F5, and LMX-F6 samples are similar to the type III adsorption isothermal, although all of them also belong to type IV(a). The hysteresis loop also changes more significantly with increasing temperature. The hysteresis loop of the adsorption isotherms of samples LMX-FS, LMX-F1, LMX-F2 and LMX-F3 are all of type H4. The hysteresis loops of the adsorption isothermal of samples LMX-F4, LMX-F5, and LMX-F6 are all H3 type. The adsorption capacity of liquid nitrogen by mesopores shows a decreasing and then increasing trend.

High-pressure mercury injection experiment is one of the most



Fig. 3. The process of experimentation and analysis.

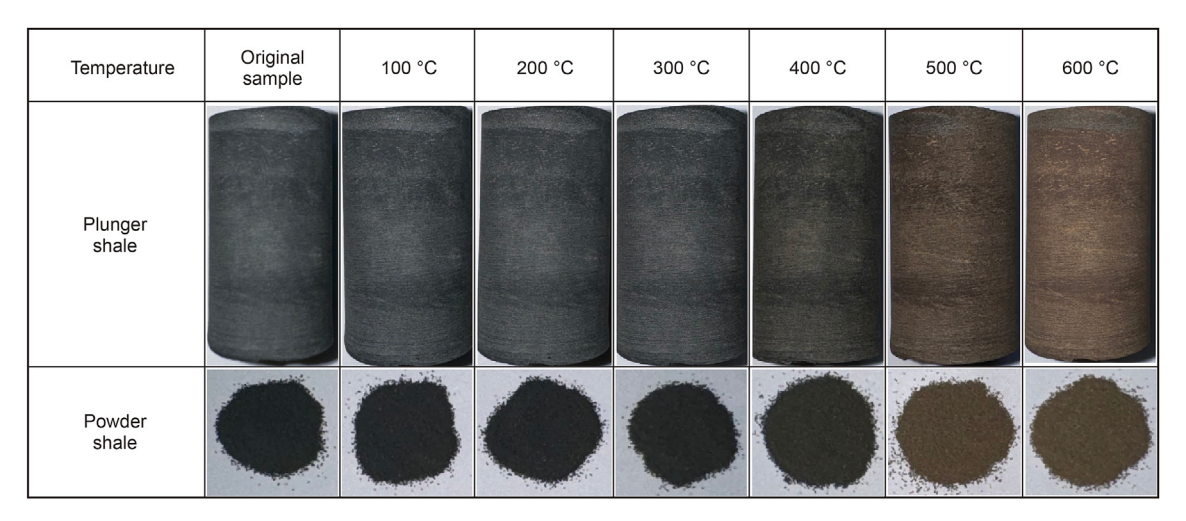


Fig. 4. Color changes of plunger shale and powder shale.

important methods to characterise the pore structure. The results of the high-pressure mercury injection experiment indicate that with the increase of injection pressure, the amount of mercury in the Longmaxi Formation shale increases rapidly, then the amount of mercury tends to stabilise, and then the amount of mercury in the Longmaxi Formation shale increases rapidly again with the further increase of pressure (Fig. 9). The mercury compression

curves are classified into two types according to their characteristics. The mercury injection—withdrawal curves of LMX-FS, LMX-F1, LMX-F2, LMX-F3, LMX-F4, and LMX-F5 samples are type I. The mercury injection—withdrawal curve of LMX-F6 sample is type II. The difference between the two types of curves is that there is a significant difference between the discharge pressure and the amount of mercury feed. For Type I, the discharge pressure is large

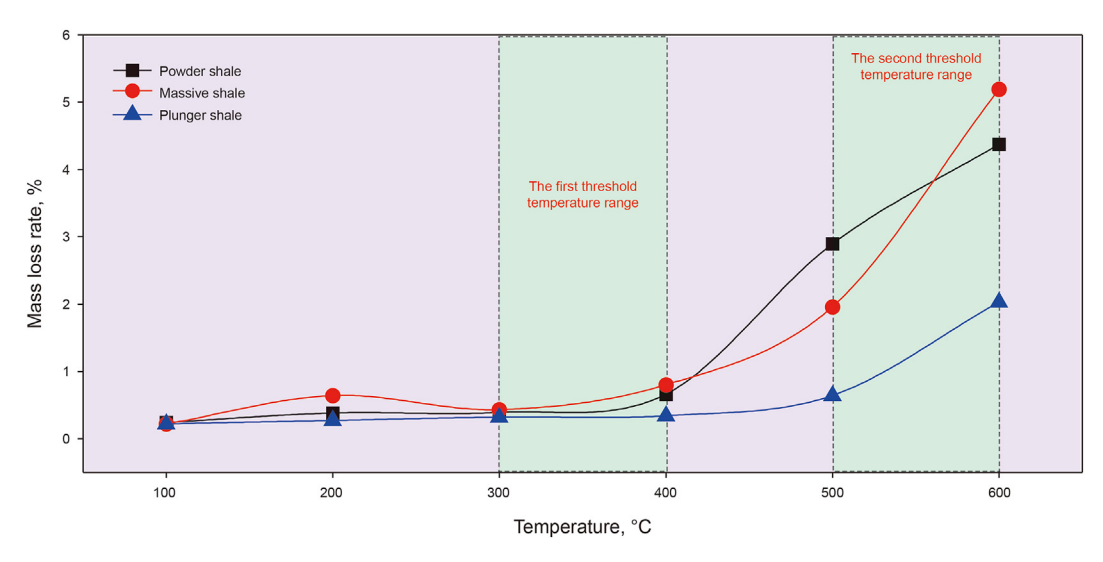


Fig. 5. Mass loss rates of plunger shale, massive shale, and powder shale.

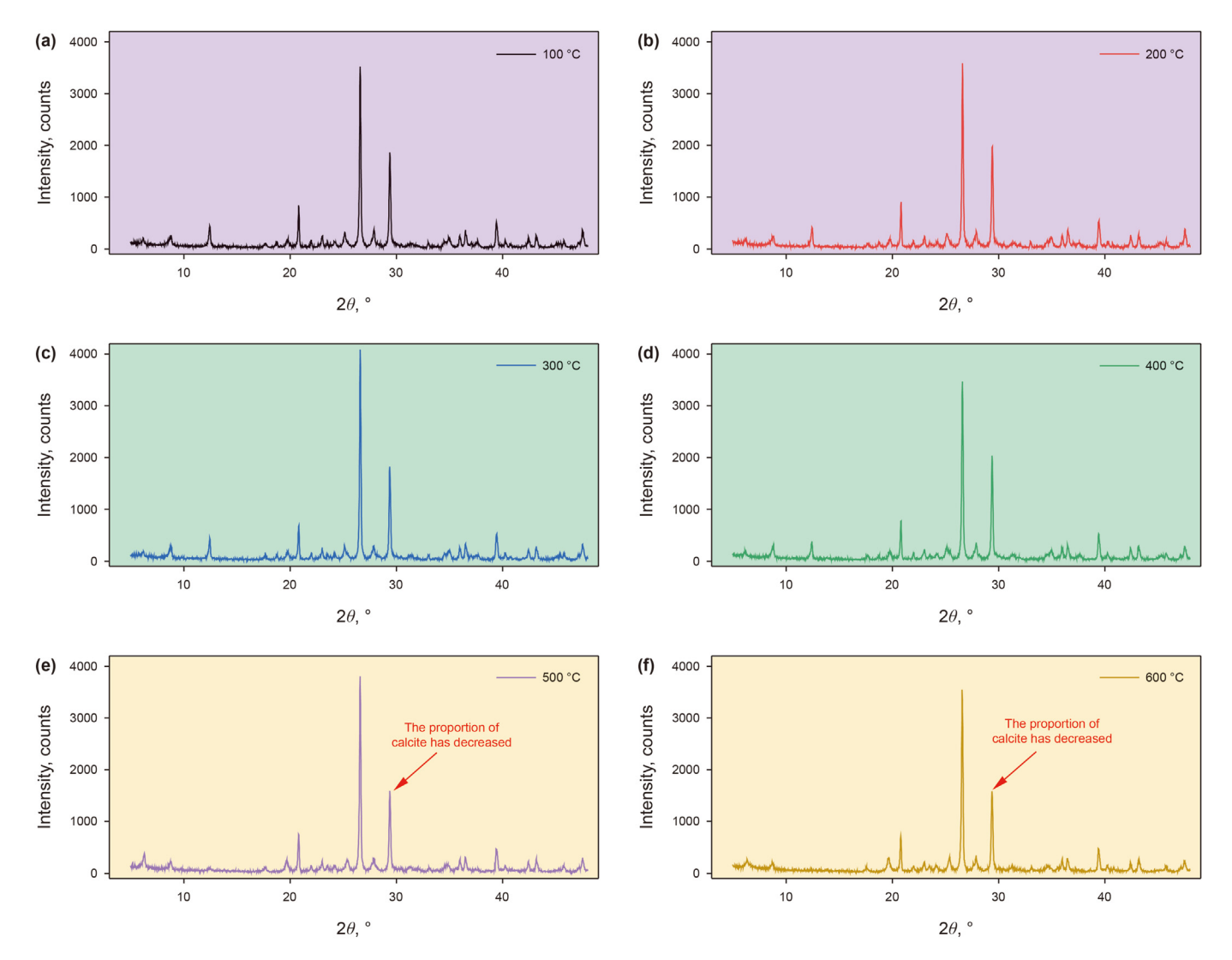


Fig. 6. Mineral composition of shale samples after thermal treatment.

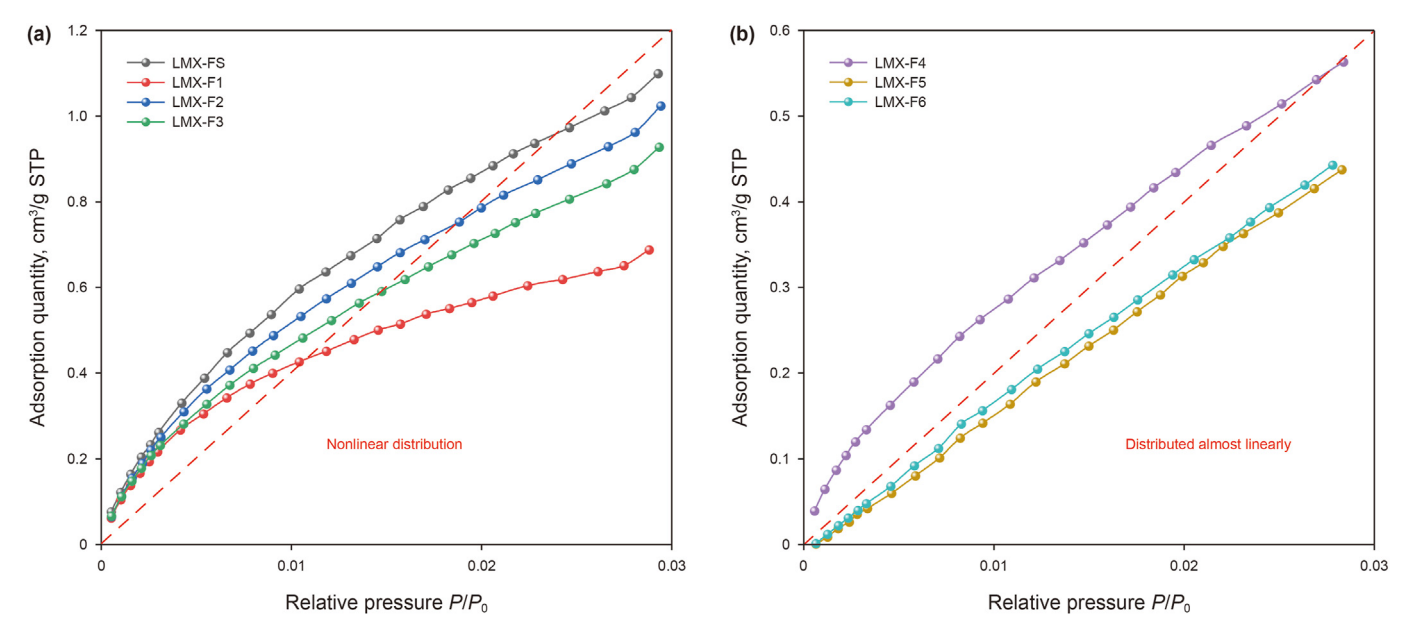


Fig. 7. Changes in carbon dioxide adsorption curves.

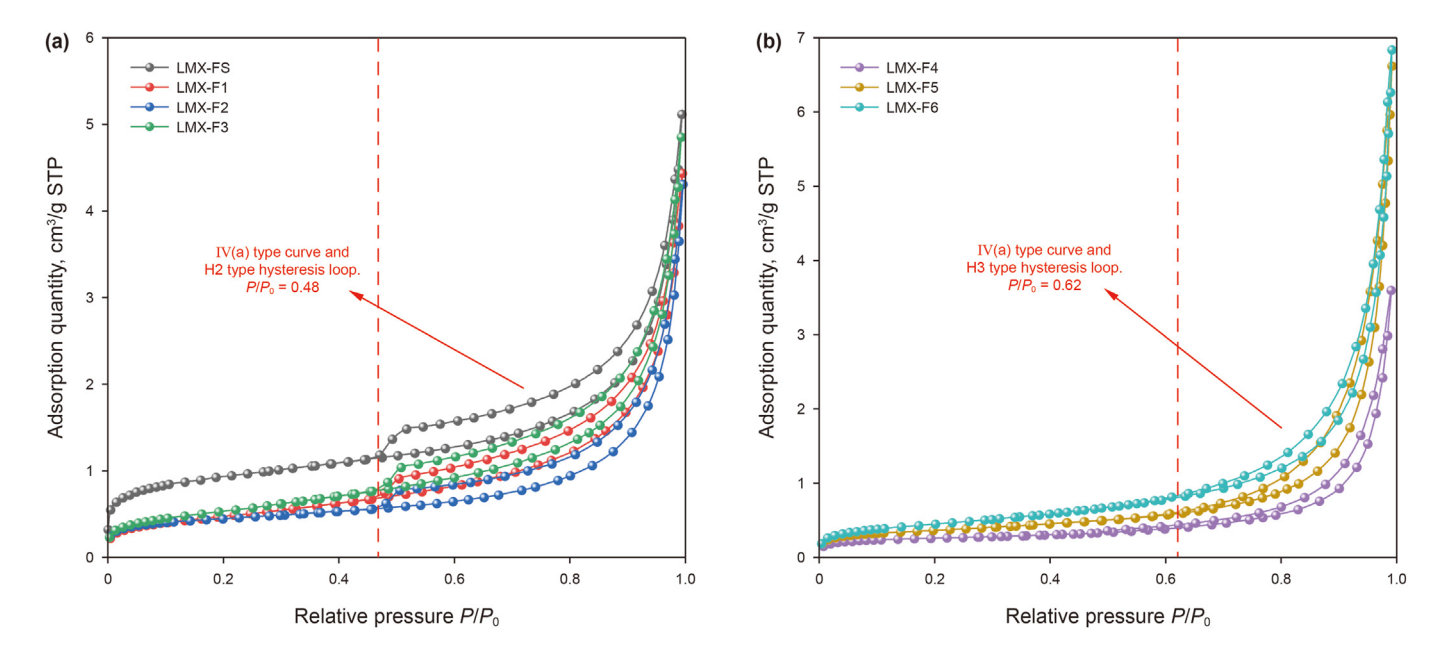


Fig. 8. Changes in liquid nitrogen adsorption curves.

and the amount of mercury feed is small. On the contrary, Type II has a small discharge pressure and a large amount of mercury feed.

3.3. Modelling of fluid-structure interaction simulations

FIB-SEM technology is used to obtain detailed sample sections based on CT data. This method combines the advantages of a focused ion beam and a scanning electron microscope to obtain high-resolution 2D slice images. The acquired image is preprocessed with noise cancellation and contrast adjustment to improve the image quality and make the subsequent reconstruction process more accurate. After the image preprocessing is completed, the image slices are superimposed layer by layer, and the two-dimensional image information is transformed into a three-dimensional structure through interpolation and

reconstruction techniques. The pores are segmented using the threshold segmentation method. The porosity and connectivity are calculated, and a 3D model of the porosity is established. Next, the maximum ball method is used to construct the bat. Finally, the absolute permeability is calculated to establish the fluid model (Fig. 10).

4. Discussion

4.1. Changes in the structure of pore-fractures

The shale samples after treatment at 100, 200, and 300 °C did not have significant structural changes, except for the microporosity in the organic matter. This phenomenon has also been discovered by several scholars and pointed out that there are three

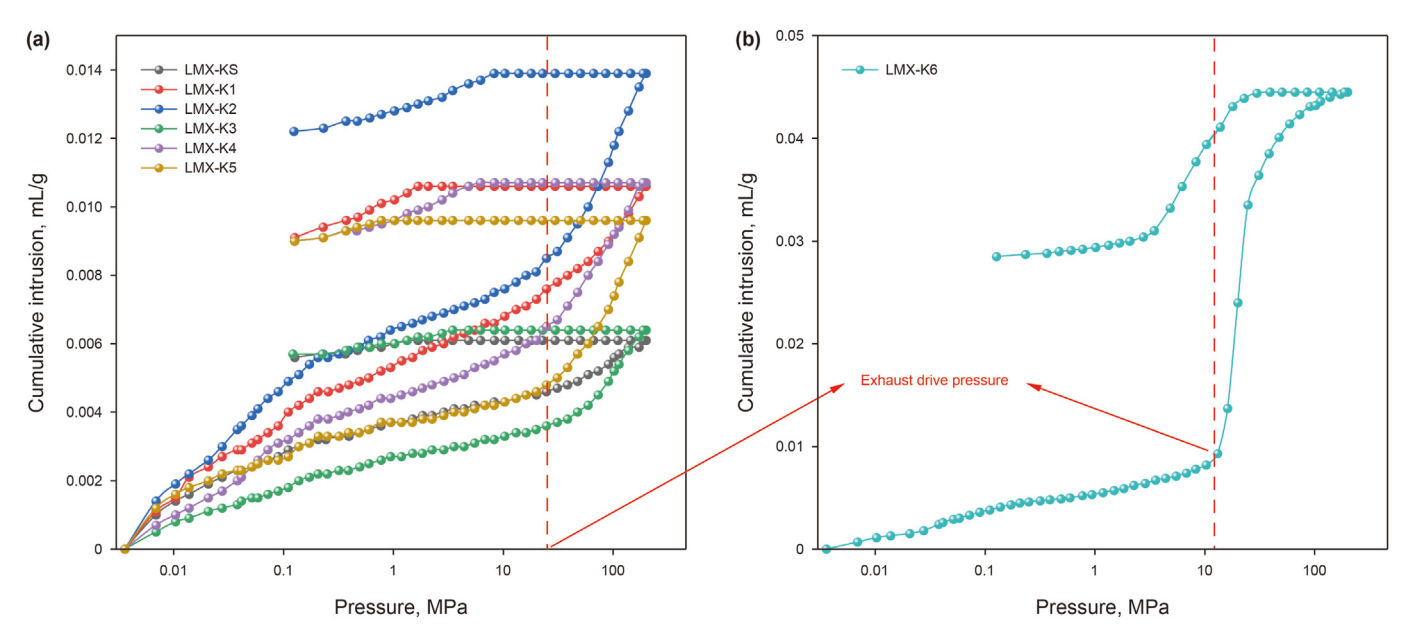


Fig. 9. Changes in high-pressure mercury pressure curves.

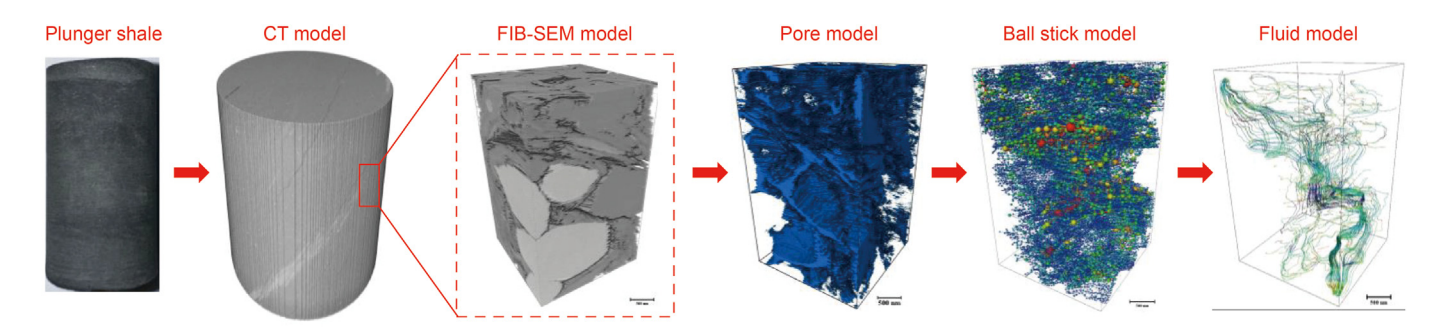


Fig. 10. Process for modelling fluid-structure interaction simulations.

main reasons for the formation of pore-fracture before 300 °C (Jia et al., 2024; Li et al., 2019; Liu et al., 2021). First, the organic matter of some saprolite groups with high hydrocarbon generation potential releases oil and gas during the heating process, resulting in micropores. Second, the contact area between organic matter and minerals will be affected by temperature, resulting in thermal fracture of minerals and the formation of edge thermal rupture effect. Third, clay minerals will undergo dehydration when exposed to heat, resulting in shrinkage and deformation, forming fractures. Therefore, the newly created pore-fractures before 300 °C are mainly caused by thermal rupture of mineral edges and hydrocarbon emissions from organic matter (Fig. 11(a), (b), (d), and (e)). However, the content of clay minerals of the Longmaxi Formation shale studied in this paper is high. Pores and fractures are generated in the area of dense distribution of clay minerals, but the volume expansion of clay minerals also leads to the contraction phenomenon of some fractures (Fig. 11(c) and (f)).

The pore-fracture of the shale sample changed significantly after treatment at 400 $^{\circ}$ C. There were independent strip fractures generated and organic matter was heavily pyrolysed. It is difficult to observe large organic matter under the SEM (Fig. 12(a)). Penetrated fractures were developed in the shale after treatment at 500 $^{\circ}$ C, which resulted in better pore connectivity (Fig. 12(b)). The organic matter of the shale samples after treatment at 600 $^{\circ}$ C was almost completely pyrolysed and a large number of micron-sized pores and

fractures were generated. The various pore-fractures intersect each other, which leads to a continuous increase in pore connectivity (Fig. 12(c)). Thermal decomposition between different minerals, such as clay, quartz, and feldspar, produces micron-sized fractures, which are interconnected to form a network of fractures (Cao et al., 2016; Chalmers et al., 2012) (Fig. 12(d)). The above experimental results prove that there is a threshold temperature between 300 and 400 °C, which makes the pore and fracture begin to develop in large quantities. There is a threshold temperature between 500 and 600 °C that makes the pore and fracture connectivity better, which may have a great effect on the permeability of shale.

4.2. Evolution of the distribution characteristics of the pore size

Based on the classic pore classification scheme from previous studies and IUPAC, and considering the structural characteristics of the research samples, this study divides the pores into three types (Loucks et al., 2012; Rouquerol et al., 2013; Slatt and O'Brien, 2011). Pores within the range of 0–2 nm are classified as micropores, pores in the range of 2–10 nm are mesopores, and pores larger than 10 nm are macropores. Micropores are characterized by low-temperature CO_2 adsorption experiments, mesopores are characterized by low-temperature nitrogen adsorption experiments, and macropores are characterized by high-pressure mercury intrusion experiments.

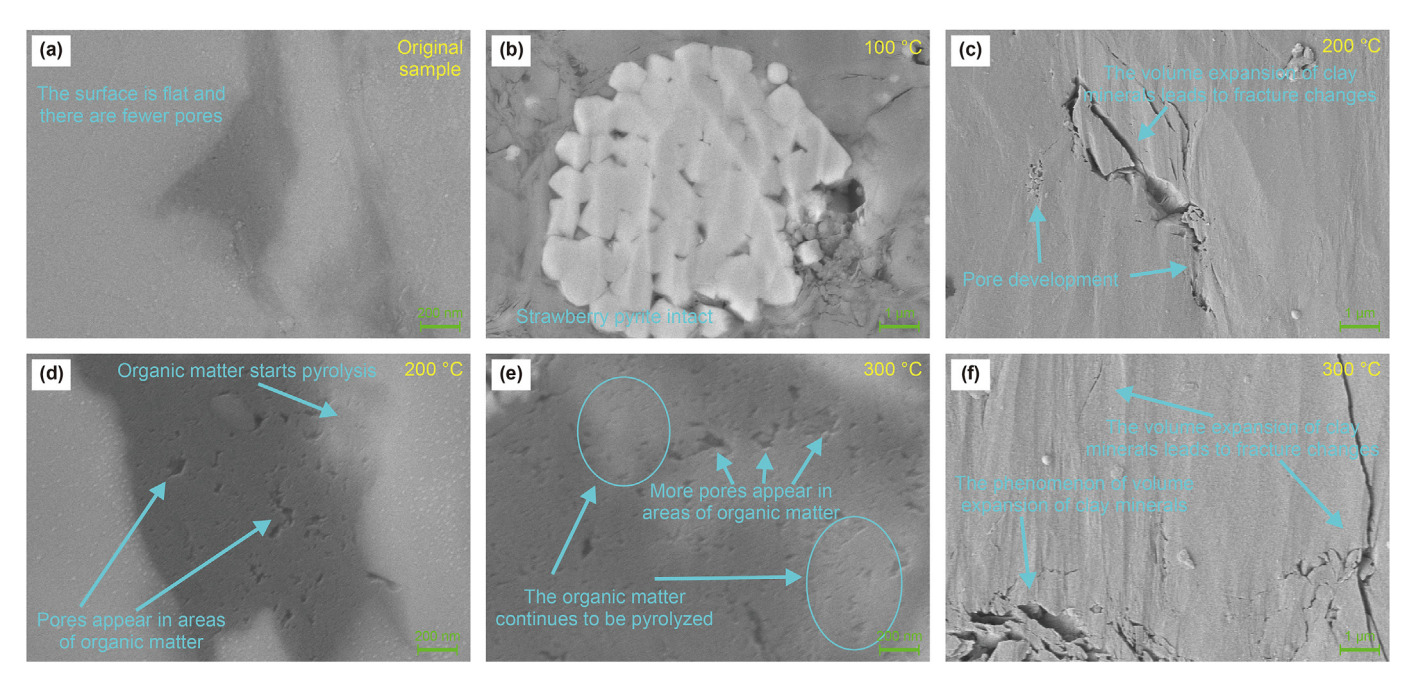


Fig. 11. SEM images of the original sample and the samples after treatment at 100, 200 and 300 °C.

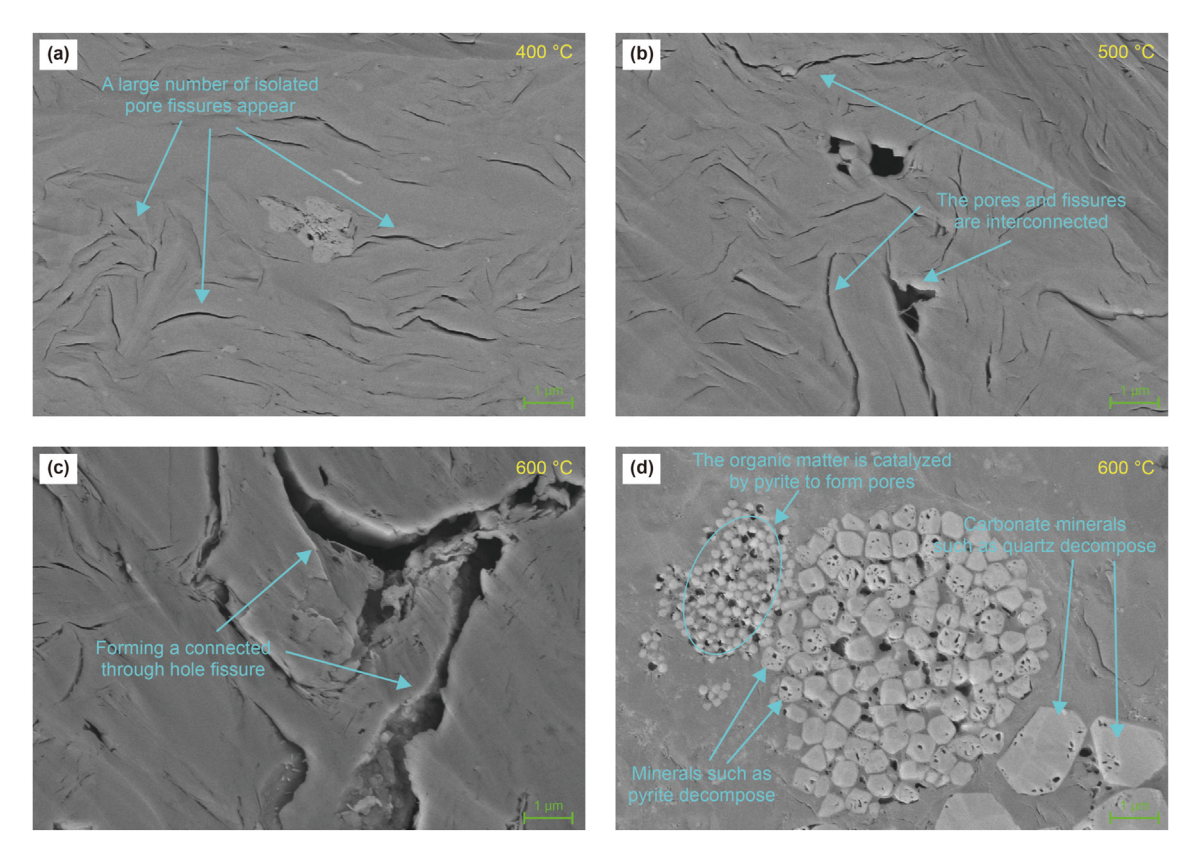


Fig. 12. SEM images of the samples after treatment at 400, 500 and 600 $^{\circ}$ C.

As shown in Fig. 13(a), there is a significant pattern of change in the microporous pore size distribution characteristics with increasing temperature. The percentage of micropores in shale decreases after treatment at $100\,^{\circ}$ C. The percentage of micropores in shale increases after high-temperature treatment at $200\,^{\circ}$ C. The percentage of micropores of shale decreases after high-

temperature treatment at 200, 300, 400, 500, and 600 $^{\circ}$ C. The pattern of change of microporous pore size is exactly the same as that of adsorption amount in the adsorption curve of low-temperature carbon dioxide experiment, which is also in line with the law that the curve type transforms from non-linear to linear (Figs. 7 and 13(a)). The above results indicate that the

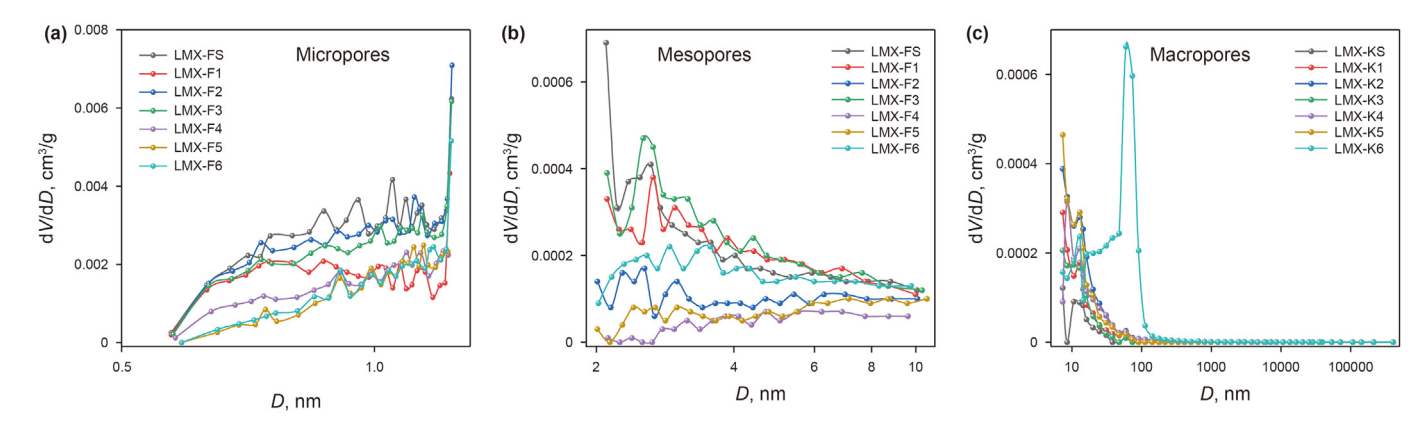


Fig. 13. Pore size distribution.

micropores become less and less as the temperature rises, resulting in a weaker and weaker $\rm CO_2$ adsorption capacity of the shale after high temperature treatment. There exists a threshold temperature between 300 and 400 °C, which makes the percentage of microporosity decrease suddenly, and there is almost no microporosity after 500 °C. It can be inferred that a large number of micropores are transformed to mesopores under the influence of the threshold temperature.

As shown in Fig. 13(b), there is also a relatively pattern of changes in mesopore pore size distribution characteristics with increasing temperature. The percentage of mesopores in the shale after treatment at 200 °C decreases. The percentage of mesopores in the shale after treatment at 300 °C increases. The percentage of mesopores in shale after treatment at 400 °C decreases. The percentage of mesopores increases after treament at 500 and 600 °C. The pattern of change in the percentage of mesopore size is exactly the same as that of the adsorption-desorption curves of the lowtemperature liquid nitrogen experiments, which is also in line with the pattern of the transition of the hysteresis loop from the H4 type to the H3 type, and that of the adsorption curves from the IV(a) type to the III type (Figs. 8 and 13(b)). The above experimental results indicate that the pore size becomes larger and the pore type changes from complex to simple with the temperature increase. This leads to a gradual shift from micro/mesoporous materials to

medium- to macroporous materials in the shale after high-temperature treatment. There is a threshold temperature between 500 and 600 °C, which causes a sudden increase in the percentage of mesopores, and a large number of mesopores are transformed to macropores under the influence of the threshold temperature.

As shown in Fig. 13(c), the characteristic change of macroporous pore size distribution does not change significantly, but it still coincides with the change pattern of the results of the high-pressure mercury experiment. The percentage of macropores in the shale after treatment at 200 °C increases. The percentage of macropores in the shale after treatment at 300 °C decreases. The macroporosity of shale treated at 400 and 500 °C increases. The above experimental results prove that there is a threshold temperature between 300 and 400 °C that makes the percentage of macropores start to increase, and there is a threshold temperature between 500 and 600 °C that makes the percentage of macropores increase significantly. The pattern of change of macroporous pore size ratio is exactly the same as that of the high-pressure Hg-pressure experiments, which is also in accordance with the change of the Hgpressure curve from type I to type II (Figs. 9 and 13(c)). It proves that there exists a threshold temperature between 500 and 600 °C, which causes a sudden increase in the percentage of macropores. And the type I curve shows that the volume difference and the

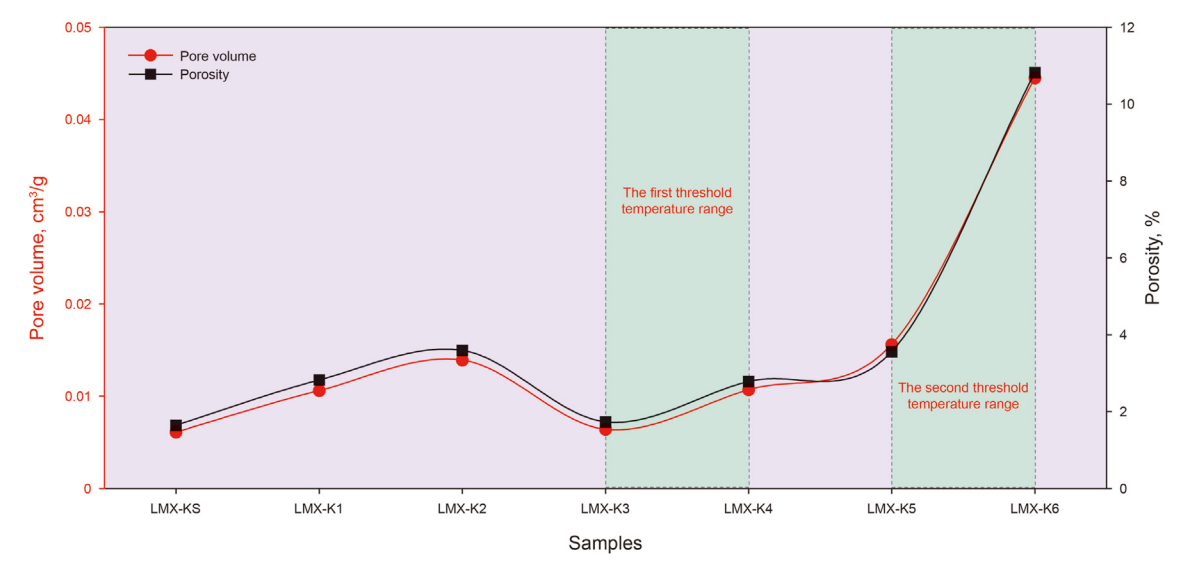


Fig. 14. Variations of pore volume and porosity.

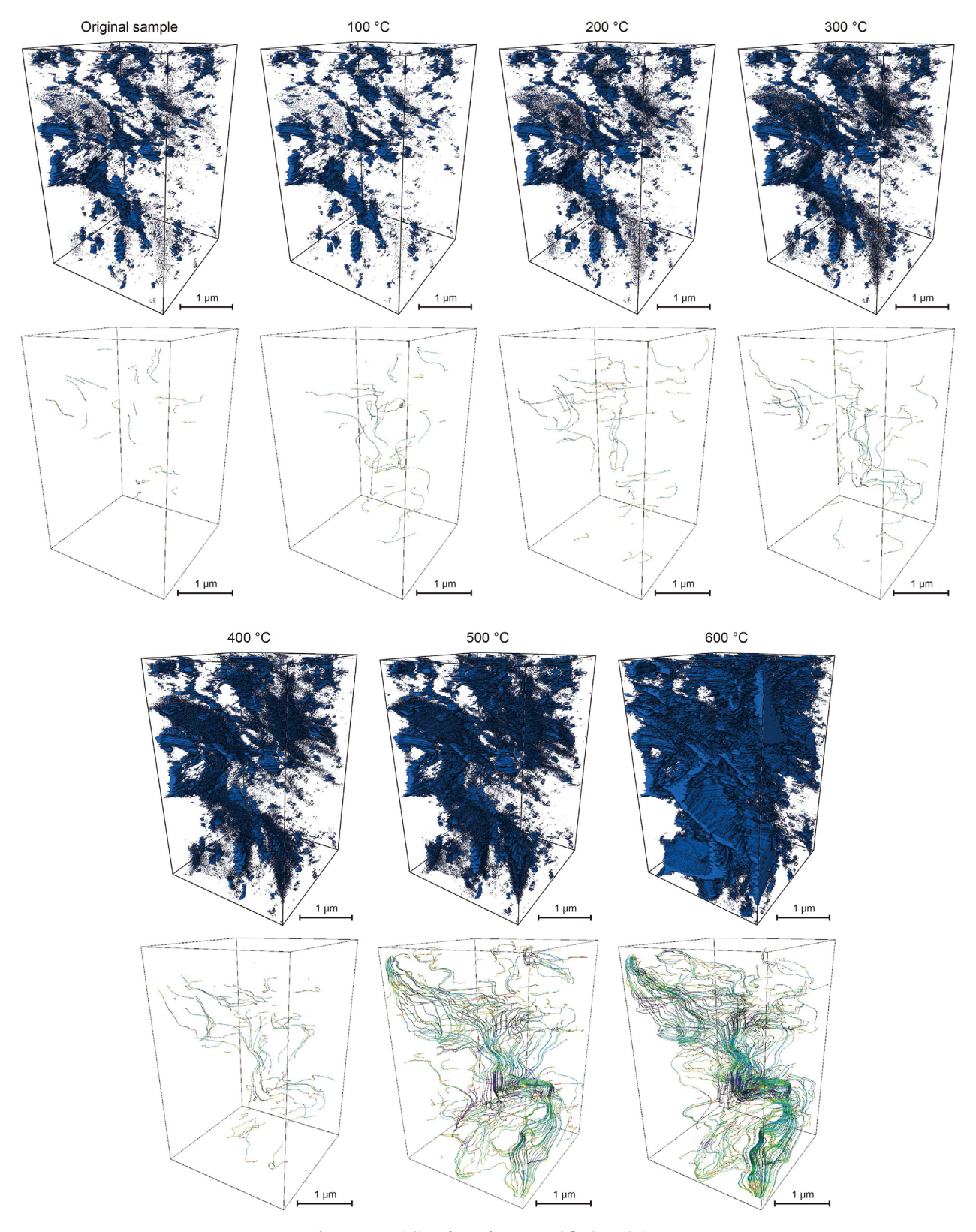


Fig. 15. 3D modeling of pore-fractures and fluid simulation.

expulsion pressure between entering and exiting mercury are larger. It shows that the pore structure is complex, the overall pore size is small, the pore connectivity is poor, and the non-homogeneity is strong. However, under the influence of threshold

temperature, the pore structure becomes simple and homogeneous, and the pore connectivity becomes better.

The variations of pore volume and porosity coincide with the trend of the high-pressure mercury pressure curve and the results

of the SEM experiments (Fig. 14). Specifically, the pore volume and porosity of macropores increase before 200 °C. It is possible that the high content of clay minerals in the mineral fraction leads to an increase in the pore volume and porosity of the macropores after the high temperature treatment at 200 °C and a decrease in the pore volume and porosity of the macropores after the high temperature treatment at 300 °C. Several scholars believe that different minerals have different expansion characteristics, and that there are different physical and chemical changes in the minerals inside the rock at high temperatures (Sirdesai et al., 2017). The results of Xiong et al. (2023) showed that the porosity of mudstone with high clay mineral content also tends to decrease in the stage of 200-300 °C. Between 300 and 500 °C, the pore volume and porosity of macropores increase, which suggests that a threshold temperature between 300 and 400 °C causes the pore volume and porosity of macropores to rise. Another threshold temperature between 500 and 600 °C significantly increases the pore volume and porosity of macropores. This is also consistent with the conclusions obtained through the scanning electron microscopy imaging method.

4.3. Analysis of fluid-structure interaction

CT, FIB-SEM techniques and coupled fluid—structure interaction simulation methods were used to further analyse the effect of temperature on shale pore structure. Shale 3D models, poresplitting models, fluid models, pore-fracture occupancy (sum of porosity and fracture occupancy), and absolute permeability were used to qualitatively and quantitatively characterise the structural changes in shale.

The pore 3D maps of the original samples, the samples after treatment at 100, 200 and 300 °C show that the pores are small and isolated (Fig. 15), and the pore-fracture ratios are 3.82%, 4.56%, 4.22% and 5.76%, respectively (Fig. 16). The fluid simulation results show little connectivity within shale, which indicates that the pore-fracture of the shale is mainly dominated by isolated pores and isolated fracture. The connectivity between the pores and fractures is poor, which cannot form an effective hydrocarbon channel.

The shale after treatment at 200 $^{\circ}$ C shows a decrease in the pore-fracture percentage and a continued increase in absolute permeability, which could be caused by the higher clay mineral content. Although the pore size distribution indicates that the percentage of both micropores and macropores increases at 200 $^{\circ}$ C (Fig. 13(a) and (c)), and the overall porosity shows an upward trend

(Fig. 14). However, volume expansion of clay minerals leads to fracture shrinkage, which can cause a decreasing trend in the pore-fracture percentage (Fig. 11(c) and (f)). The enhanced permeability is attributed to improved pore connectivity, and the fluid simulation results show that there are more streamlines appearing with increasing temperature, which indicates that the internal connectivity of the shale is better with increasing temperature (Fig. 15).

The pore-fracture ratio of the shale after treatment at 400 °C is 8.36%, which increases by 45% and the permeability grows by 27% compared with that of the shale after treatment at 300 °C (Fig. 16). The growth rate of pore-fracture degree becomes larger, while the absolute permeability does not increase significantly. The 3D model of the pores shows a significant increase in the percentage of pores, but the fluid simulation results indicate that the number of streamlines inside the shale remains low (Fig. 15), which indicates that there are still a large number of isolated pores in the pore structure. The above results are consistent with the results of scanning electron microscopy experiments and fluid injection experiments, and are also similar to the findings of other scholars (Wang et al., 2020). The pore-fracture degree of the shale after treatment at 500 °C is 11.57%, which is a 38% increase in porefracture degree and a 56% increase in permeability compared to the sample after treatment at 400 °C. The three-dimensional modelling of the pore space shows a further increase in the percentage of pore space. The fluid simulation results show a large number of flow lines appearing. The above results demonstrate that the pore-fracture number, pore-fracture percentage and connectivity have increased substantially.

The permeability, porosity, and weight of the samples treated at 600 °C show significant changes. The porosity increases by 57%, and the permeability increases by 76% (Fig. 16). There are two main reasons for the significant increase in the proportion of porefracture and connectivity. First, the properties of quartz change, with quartz undergoing an α - β transition at 573 °C. The density of quartz in the β phase decreases, and its volume increases. Second, there is the complete pyrolysis of organic matter and the massive decomposition of carbonate minerals. According to the research of Xiong et al. (2023), shale organic matter releases some organic acids during high-temperature pyrolysis. Organic acids accelerate the decomposition of carbonate minerals, as well as clay minerals, pyrite, and other minerals. As a result, the organic matter of the samples treated at 600 °C is almost completely pyrolysed and the carbonate minerals are greatly reduced, which causes a large number of pores and fractures to be generated. The β -phase quartz

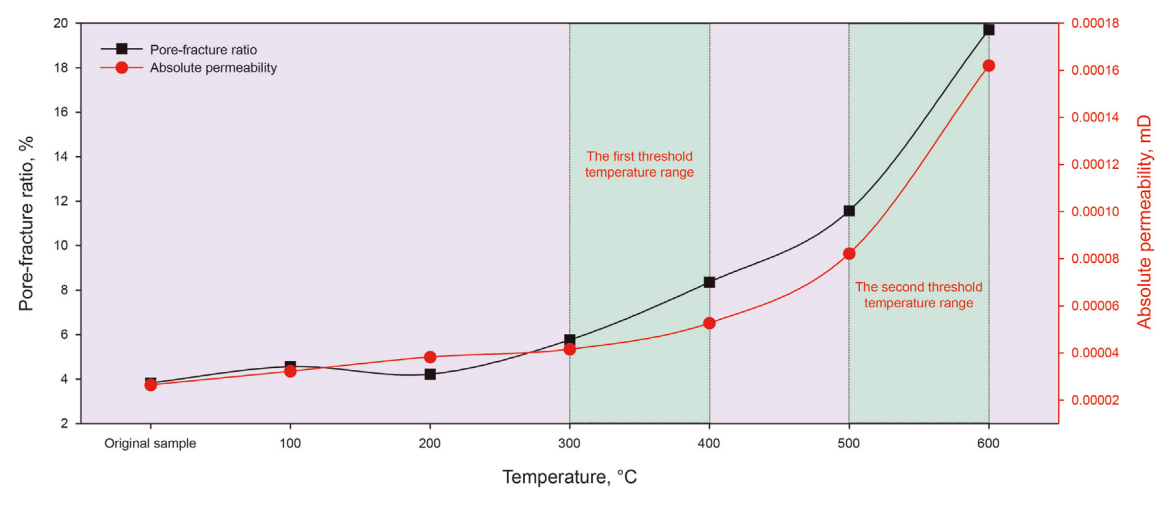


Fig. 16. Changes in absolute permeability and pore-fracture ratio.

again transforms into α -phase quartz as the temperature decreases. The reduction of quartz volume causes further increase of pore-slit between minerals, which leads to a substantial increase of pore-slit ratio and connectivity. The results of pore space 3D modelling and fluid simulation show that the pore-slit ratio is greatly increased, and more and coarser streamlines appear inside the shale (Fig. 15). It is proved that the existence of a threshold temperature between 500 and 600 °C is very helpful to increase the permeability of Longmaxi Formation shale.

5. Conclusions

The study reveals the structural changes of Longmaxi Formation shale under high temperatures through physical experiments and fluid—structure interaction simulations. In the experiment, powdered shale samples and fluid injection experiments were used to quantitatively characterise the changes in shale structure. Massive shale samples and scanning electron microscope (SEM) experiments were used to qualitatively characterise the changes in shale pore-fracture morphology. CT, FIB-SEM, and fluid—structure interaction simulation were used to comprehensively characterise the changes in pore-fracture ratio, permeability and fluid patterns within the shale. Combining the above experimental results to analyse the threshold temperature range that makes the structure of shale change at high temperature. The following conclusions were drawn.

- (1) The colour, mass, pore-fracture characteristics, and permeability of the shale do not change significantly until 300 °C. The shale is also found to have a high porosity and a low permeability. The results of scanning electron microscopy experiments indicate that the new pores in the shale are mainly formed due to the pyrolysis of organic matter. The three-dimensional model of the pores shows a low pore-fracture percentage and almost no fluid lines inside the fluid model. However, it is found that there are two threshold temperatures within the range of 300 to 600 °C that have a large effect on the structure and permeability of the shale.
- (2) The first threshold temperature is between 300 and 400 °C, which causes the shale colour to change from dark black to light grey, the organic matter to start pyrolysis, the mass loss rate to increase, the porosity to increase and the porefracture ratio to start increasing. The mass loss rates of powder shale, massive shale and plunger shale samples increase from 0.39%, 0.43% and 0.01% to 0.66%, 0.80% and 0.34%, respectively. The pore size distribution results show a decrease in micropores and mesopores and an increase in macropores. Although the porosity and pore fracture percentage increase from 1.73% and 5.76% to 2.78% and 8.36%, respectively, they have little effect on the permeability. Scanning electron microscope images, pore 3D models, and fluid models show that the generated pore-fractures are isolated, which proves that the internal connectivity of the shale is still poor.
- (3) The second threshold temperature is between 500 and 600 °C, which causes the colour of the oil shale to change from light grey to yellowish and the organic matter to be almost completely pyrolysed. The mass loss rate, porosity, and pore-fracture ratio of the shale increase sharply. The mass loss rates of powdered shale samples, massive shale samples, and plunger shale samples increase from 2.89%, 1.96%, and 0.64% to 4.37%, 5.19%, and 2.03%, respectively. The pore size distribution indicates a reduction in the number of micropores and an increase in mesopores and macropores. The porosity and pore-fracture ratio increases from 3.56%

and 11.57% to 19.70% and 8.36%, respectively, and the permeability increases by 6.13 times of the original sample. Scanning electron microscopy images, pore 3D models, and fluid models indicate that a large number of interconnected pore-fractures are generated, which makes the shale internally extremely well connected. It is demonstrated that the permeability of the shale after threshold temperature treatment is greatly improved.

CRediT authorship contribution statement

Xiang-Ru Chen: Writing — review & editing, Writing — original draft, Funding acquisition, Formal analysis, Data curation, Conceptualization. **Xin Tang:** Writing — review & editing, Validation, Supervision, Resources, Funding acquisition. **Rui-Gang Zhang:** Writing — review & editing, Validation, Supervision, Software, Project administration, Methodology, Investigation. **Heng Yang:** Resources, Project administration, Methodology, Investigation. **Qiu-Qi Chen:** Methodology, Investigation, Funding acquisition. **Zhang-Ping Yan:** Validation, Supervision, Software, Funding acquisition. **Lei Zhang:** Supervision, Project administration, Investigation.

Declaration of interest statement

The authors declare that they have no known competing financial interests or personal relationships, which will not affect the work reported in this article.

Acknowledgements

This research was supported by the Chongqing Natural Science Foundation of Chongqing, China (No. CSTB2022NSCQ-MSX0333), the Science and Technology Research Program of Chongqing Municipal Education Commission (Grant No. KJZD-K202401205), Chongqing Three Gorges University Graduate Research and Innovation Project Funding (No. YJSKY24045), Chongqing Engineering Research Center of Disaster Prevention & Control for Banks and Structures in Three Gorges Reservoir Area (No. SXAPGC24YB14, No. SXAPGC24YB03, No. SXAPGC24YB12).

References

- Altun, N.E., Hicyilmaz, C., Wang, J.Y., et al., 2006. Oil shales in the world and Turkey; reserves, current situation and future prospects: A review. Oil Shale 23 (3), 211–227. https://doi.org/10.3176/oil.2006.3.02.
- Bera, A., Babadagli, T., 2015. Status of electromagnetic heating for enhanced heavy oil/bitumen recovery and future prospects: A review. Appl. Energy 151, 206–226. https://doi.org/10.1016/j.apenergy.2015.04.031.
- Burnham, A.K., 2016. A simple kinetic model of oil generation, vaporization, coking, and cracking. Energy Fuels 30 (3). https://doi.org/10.1021/acs.energy-fuels.5b02026. 2524-2524.
- Burnham, A.K., 2018. Thermomechanical properties of the garden gulch member of the green river formation. Fuel 219, 477–491. https://doi.org/10.1016/i.fuel_2018.01.122.
- Cao, P., Liu, J.S., Leong, Y.K., 2016. A fully coupled multiscale shale deformation-gas transport model for the evaluation of shale gas extraction. Fuel 178, 103—117. https://doi.org/10.1016/j.fuel.2016.03.055.
- Chalmers, G.R.L., Ross, D.J.K., Bustin, R.M., 2012. Geological controls on matrix permeability of Devonian Gas Shales in the Horn River and Liard basins, northeastern British Columbia, Canada. Int. J. Coal Geol. 103, 120–131. https://doi.org/10.1016/j.coal.2012.05.006.
- Chang, X., Wang, X.Y., Yang, C.H., et al., 2024. Experimental investigation on mode I fracture characteristics of Longmaxi formation shale after cyclic thermal shock and high-temperature acid etching treatments. Eng. Fract. Mech. 295, 109762. https://doi.org/10.1016/j.engfracmech.2023.109762.
- Chen, X.R., Tang, X., Liu, C., et al., 2024. Implications of temperature for the modification of high-overmature shale reservoirs: Experimental and numerical analysis. SPE J. 29 (8), 4218–4231. https://doi.org/10.2118/219762-PA.
- Gavrilova, O., Vilu, R., Vallner, L., 2010. A life cycle environmental impact assessment

- of oil shale produced and consumed in Estonia. Resour. Conserv. Recycl. 55 (2), 232–245. https://doi.org/10.1016/j.resconrec.2010.09.013.
- Han, J., Sun, Y.H., Guo, W., et al., 2019. Characterization of pyrolysis of nong'an oil shale at different temperatures and analysis of pyrolysate. Oil Shale 36 (2), 151–170. https://doi.org/10.3176/OIL.2019.25.06.
- Han, X.X., Niu, M.T., Jiang, X.M., 2014. Combined fluidized bed retorting and circulating fluidized bed combustion system of oil shale: 2. Energy and economic analysis. Energy 74, 788–794. https://doi.org/10.1016/i.energy.2014.07.050.
- Jia, Y.C., Huang, X.D., Yang, D., et al., 2024. Thermo-hydro-mechanical coupling in oil shale: Investigating permeability and heat transfer under high-temperature steam injection. Case Stud. Therm. Eng. 61, 104862. https://doi.org/10.1016/ i.csite.2024.104862.
- Jiang, X.M., Han, X.X., Cui, Z.G., 2007. New technology for the comprehensive utilization of Chinese oil shale resources. Energy 32 (5), 772–777. https://doi.org/10.1016/j.energy.2006.05.001.
- Kang, Z.Q., Li, X., Yang, T., et al., 2018. Comparisons of pore structures of oil shale upon conduction and convection heating. Chin. J. Rock Mech. Eng. 37 (11), 2565–2575. https://link.cnki.net/doi/10.13722/j.cnki.jrme.2018.0651 (in Chinese).
- Kang, Z.Q., Zhao, Y.S., Yang, D., 2020. Review of oil shale in-situ conversion technology. Appl. Energy 269, 115121. https://doi.org/10.1016/j.apenergy.2020.115121.
- Kang, Z.Q., Jiang, X., Wang, L., et al., 2023. Comparative investigation of in situ hydraulic fracturing and high-temperature steam fracturing tests for meterscale oil shale. Energy 281, 128343. https://doi.org/10.1016/ j.energy.2023.128343.
- Kim, T.W., Ross, C.M., Guan, K.M., et al., 2020. Permeability and porosity evolution of organic-rich shales from the Green River Formation as a result of maturation. SPE J. 25 (3), 1377–1405. https://doi.org/10.2118/195366-PA.
- Lee, K.J., Moridis, G.J., Ehlig-Economides, C.A., 2017. Compositional simulation of hydrocarbon recovery from oil shale reservoirs with diverse initial saturations of fluid phases by various thermal processes. Energy Explor. Exploit. 35 (2), 172–193. https://doi.org/10.1177/0144598716684307.
- Lei, J., Pan, B.Z., Guo, Y.H., et al., 2021. A comprehensive analysis of the pyrolysis effects on oil shale pore structures at multiscale using different measurement methods. Energy 227 (1), 120359. https://doi.org/10.1016/j.energy.2021.120359.
- Li, J.Z., Dong, D.Z., Chen, G.S., et al., 2009. Prospects and strategic position of shale gas resources in China. Nat. Gas. Ind. 29 (5), 7–10. https://doi.org/10.3787/j.issn. 1000-0976.2009.05.002. (in Chinese).
- Li, Y., Lin, B.Q., Yang, K., et al., 2019. Evolution law of microscopic pore fractures of coal after hot steam injection. Coal Sci. Technol. 47 (12), 102–108. https://link.cnki.net/doi/10.13199/j.cnki.cst.2019.12.014.
- Lin, L.X., Lai, D.G., Guo, E., et al., 2016. Oil shale pyrolysis in indirectly heated fixed bed with metallic plates of heating enhancement. Fuel 163, 48–55. https:// doi.org/10.1016/j.fuel.2015.09.024.
- Liu, J., Yao, Y.B., Elsworth, D., 2024. Morphological complexity and azimuthal disorder of evolving pore space in low-maturity oil shale during in-situ thermal upgrading and impacts on permeability. Pet. Sci. 21 (5), 3350–3362. https://doi.org/10.1016/j.petsci.2024.03.020.
- Liu, S.Q., Wang, H., Wang, R., et al., 2021. Research advances on characteristics of pores and fractures in coal seams. Acta Sedimentol. Sin. 39 (1), 212–230. https://link.cnki.net/doi/10.14027/j.issn.1000-0550.2020.064 (in Chinese).
- Liu, Z.J., Yang, D., Hu, Y.Q., et al., 2018. Influence of in situ pyrolysis on the evolution of pore structure of oil shale. Energies 11 (4), 755. https://doi.org/10.3390/ en11040755.
- Loucks, R.G., Reed, R.M., Ruppel, S.C., et al., 2012. Spectrum of pore types and networks in mudrocks and a descriptive classification for matrix-related mudrock pores. AAPG Bull. 96 (6), 1071–1098. https://doi.org/10.1306/ 08171111061.
- Pan, Y., Zhang, X.M., Liu, S.H., et al., 2012. A review on technologies for oil shale surface retort. J. Chem. Soc. Pak. 34 (6), 1331–1338. https://doi.org/10.1016/ j.energy.2014.07.050.
- Pan, Y., Qiao, W., Chi, D.X., et al., 2024. Research of steam injection in-situ production technology to enhance unconventional oil and gas recovery: A review. J. Anal. Appl. Pyrolysis 177, 106332. https://doi.org/10.1016/j.jaap.2023.106332.
- Rouquerol, J., Avnir, D., Fairbridge, C.W., et al., 2013. Recommendations for the characterization of porous solids. J Pure and Applied Chemistry 66 (8), 1739–1758. https://doi.org/10.1351/pac199466081739 (Technical Report).
- Saif, T., Lin, Q.Y., Bijeljic, B., et al., 2017. Microstructural imaging and characterization of oil shale before and after pyrolysis. Fuel 197, 562–574. https://doi.org/ 10.1016/j.fuel.2017.02.030.
- Sirdesai, N.N., Singh, T.N., Gamage, R.P., 2017. Thermal alterations in the poro-

- mechanical characteristic of an Indian sandstone—A comparative study. Eng. Geol. 226 (1), 208–220. https://doi.org/10.1016/j.enggeo.2017.06.010.
- Slatt, R.M., O'Brien, N.R., 2011. Pore types in the Barnett and Woodford gas shales: Contribution to understanding gas storage and migration pathways in fine-grained rocks. AAPG Bull. 95 (12), 2017–2030. https://doi.org/10.1306/03301110145.
- Spigolon, A.L.D., Lewan, M.D., de Barros Penteado, H.L., et al., 2015. Evaluation of the Petroleum Composition and Quality with Increasing Thermal Maturity as Simulated by Hydrous Pyrolysis: A Case Study Using a Brazilian Source Rock with Type I Kerogen, pp. 27–53. https://doi.org/10.1016/j.orggeochem.2015.03.001, 83-84.
- Sun, B., Liu, X.P., Zhao, X.Z., et al., 2025. Laminated shale oil system mobility and controlling factors of the Paleogene Shahejie Formation: Evidences from T₁-T₂ NMR experiments, multi-temperature pyrolysis and confocal laser scanning microscopy. Fuel 379 (1), 133015. https://doi.org/10.1016/j.fuel.2024.133015.
- Sun, Y., Wang, Y.W., Liu, J.Z., et al., 2024. A pyrolysis study of kerogen and extracted bitumen from a lacustrine shale of the Shahejie Formation and implications for in-situ conversion processes. J. Anal. Appl. Pyrolysis 183 (1), 106735. https://doi.org/10.1016/j.jaap.2024.106735.
- Trikkel, A., Kuusik, R., Martins, A., et al., 2008. Utilization of Estonian oil shale semicoke. Fuel Process. Technol. 89 (8), 756–763. https://doi.org/10.1016/ ifuproc.2008.01.010.
- Velts, O., Uibu, M., Rudjak, I., et al., 2008. Utilization of oil shale ash to prepare PCC: Leachibility dynamics and equilibrium in the ash-water system. Energy Proc. 1 (1), 4843—4850. https://doi.org/10.1016/j.egypro.2009.02.312.
- Wan, T., Chen, S., Wu, X.L., et al., 2024a. An investigation on the pyrolysis of low-maturity organic shale by different high temperature fluids heating. Fuel 374 (1), 132498. https://doi.org/10.1016/j.fuel.2024.132498.
- Wan, T., Zhang, J., Wu, B.C., 2024b. NMR and CT characterizing the influence of O₂ in air injection performance in shale oil cores. Fuel 356 (1), 129639. https://doi.org/10.1016/j.fuel.2023.129639.
- Wang, L., Gao, C.H., Xiong, R.Y., et al., 2024. Development review and the prospect of oil shale in-situ catalysis conversion technology. Pet. Sci. 21 (2), 1385–1395. https://doi.org/10.1016/j.petsci.2023.08.035.
- Wang, L., S Zhao, Y., Yang, D., 2020. Investigation on meso-characteristics of in-situ pyrolysis of oil shale by injecting steam. Chin. J. Rock Mech. Eng. 39 (8), 1634–1647. https://doi.org/10.7511/jslx20211030001.
- Wang, L., Yang, D., Kang, Z.Q., 2021. Evolution of permeability and mesostructure of oil shale exposed to high-temperature water vapor. Fuel 290, 119786. https:// doi.org/10.1016/j.fuel.2020.119786.
- Wang, S., Jiang, X.M., Han, X.X., et al., 2012. Investigation of Chinese oil shale resources comprehensive utilization performance. Energy 42 (1), 224–232. https://doi.org/10.1016/j.energy.2012.03.066.
- Wei, Z.J., Sheng, J.J., 2022. Changes of pore structures and permeability of the Chang 73 medium-to-low maturity shale during in-situ heating treatment. Energy 248 (1), 123609. https://doi.org/10.1016/j.energy.2022.123609.
- Xiong, J., Zhu, M., Li, W., et al., 2023. Evolution law of physical properties of rocks with different lithologies under high temperature. Nat. Gas. Ind. 43 (12), 14–24. https://doi.org/10.3787/j.issn.1000-0976.2023.12.002. (in Chinese).
- Xu, X.H., Lu, J.L., Wang, B.H., et al., 2022. Marine basins in China: Petroleum resource dynamic evolution and exploration directions. Earth Sci. Front. 29 (6), 73–83. https://doi.org/10.13745/j.esf.sf.2022.8.21. (in Chinese).
- Yang, L.S., Yang, D., Zhao, J., et al., 2016. Changes of oil shale pore structure and permeability at different temperatureS. Oil Shale 33 (2), 101–110. https:// doi.org/10.3176/OIL.2016.2.01.
- Yu, C.S., Deng, H.C., Jiang, Q, et al., 2024. Mechanism of pore expansion and fracturing effect of high-temperature ScCO₂ on shale. Fuel 363 (1), 130950. https://doi.org/10.1016/j.fuel.2024.130950.
- Zhao, S., Xu, C.Y., Pu, W.F., et al., 2024. Feasibility of spontaneous combustion in ultra-deep high-pressure shale oil reservoirs during air injection. Thermochim. Acta 738 (1), 179783. https://doi.org/10.1016/j.tca.2024.179783.
- Zhou, Q.F., Jin, Z.J., Yang, G.F., et al., 2019. Shale oil exploration and production in the U.S.: Status and outlook. Oil Gas Geol. 40 (3), 469–477. https://doi.org/10.11743/
- Zhu, C.F., Guo, W., Sun, Y.H., et al., 2022. Reaction mechanism and reservoir simulation study of the high-temperature nitrogen injection in-situ oil shale process: A case study in Songliao Basin, China. Fuel 316, 123164. https://doi.org/10.1016/j.fuel.2022.123164.
- Zou, C.N., Zhu, R.K., Dong, D.Z., et al., 2022. Scientific and technological progress, development strategy and policy suggestion regarding shale oil and gas. Acta Pet. Sin. 43 (12), 1675–1686. https://doi.org/10.7623/syxb202212001. (in Chinese).